

upon the transgenic expression of DmDG (Fig. 2I). Among mitochondrial dehydrogenases in insects, PDH is the only enzyme that is reported to show Ca^{2+} -dependent activation (18), and therefore, it is possible that the reduced expression of DmDG causes the sustained increase in the $[\text{Ca}^{2+}]_i$, which, in turn, induces the activation of PDH, resulting in increased mitochondrial oxidative metabolism. Based on these observations, we propose that a reduction in the DmDG content initiates a chain of sequential reactions, i.e., increased membrane fluidity, activation of Ca^{2+} influx, elevated mitochondrial metabolism, and eventually, altered thermoregulatory behavior (fig. S9). It remains an enigma, however, how the metabolic changes in a cell are translated into neural code that induces behavioral change at the level of the whole animal (see also supporting online text).

References and Notes

- T. J. Crowley, G. R. North, *Science* **240**, 996 (1988).
- P. J. Mayhew, G. B. Jenkins, T. G. Benton, *Proc. Biol. Sci.* **275**, 47 (2008).
- T. H. Bullock, *Biol. Rev. Camb. Philos. Soc.* **30**, 311 (1955).
- M. J. Angilletta Jr., P. H. Niewiarowski, C. A. Navas, *J. Therm. Biol.* **27**, 249 (2002).
- I. A. Johnston, A. F. Bennett, Eds., *Animals and Temperature: Phenotypic and Evolutionary Adaptation* (Cambridge Univ. Press, Cambridge, 1996).
- C. V. Gisolfi, M. Francisco, *The Hot Brain: Survival, Temperature and the Human Body* (MIT Press, Cambridge, MA, 2000).
- B. Heinrich, *The Hot-Blooded Insects: Strategies and Mechanisms of Thermoregulation* (Harvard Univ. Press, Cambridge, MA, 1993).
- M. J. Greener, R. G. Roberts, *FEBS Lett.* **482**, 13 (2000).
- W. M. Deng et al., *Development* **130**, 173 (2003).
- M. S. Patel, L. G. Korotchkina, *Biochem. Soc. Trans.* **34**, 217 (2006).
- S. K. Kim, E. J. Rulifson, *Nature* **431**, 316 (2004).
- A. A. Steiner, L. G. Branco, *Annu. Rev. Physiol.* **64**, 263 (2002).
- S. Mahajan, N. Tuteja, *Arch. Biochem. Biophys.* **444**, 139 (2005).
- J. E. Kammenga et al., *PLoS Genet.* **3**, e34 (2007).
- J. G. McCormack, A. P. Halestrap, R. M. Denton, *Physiol. Rev.* **70**, 391 (1990).
- P. Gailly, *Biochim. Biophys. Acta* **1600**, 38 (2002).
- R. Barresi, K. P. Campbell, *J. Cell Sci.* **119**, 199 (2006).
- J. G. McCormack, R. M. Denton, *Biochem. J.* **196**, 619 (1981).
- L. Liu, O. Yermolaieva, W. A. Johnson, F. M. Abboud, M. J. Welsh, *Nat. Neurosci.* **6**, 267 (2003).
- Wild type, $7.3 \pm 1.8\%$ (mean \pm SEM); *atu* mutant, $67.3 \pm 3.7\%$; and DmDG transgenic *atu* mutant (*atu/atu*; *actin5C-GAL4/UAS-DmDG*), $7.3 \pm 1.8\%$. Error bars represent SEM ($n = 3$).
- Control *actin5C-GAL4* line (*actin5C-GAL4/+*), $15.7 \pm 4.2\%$ (mean \pm SEM); "DmDG-knockdown" line (*actin5C-GAL4/UAS-dsRNA*), $59.0 \pm 3.6\%$; and control *UAS-dsRNA* line (*+UAS-dsRNA*), $25.4 \pm 7.7\%$. Error bars represent SEM ($n = 7$).
- Wild type, 1.6 ± 0.1 (mean \pm SEM); *atu* mutant, 3.0 ± 0.1 ; and DmDG-transgenic *atu* mutant (*atu/atu*; *actin5C-GAL4/UAS-DmDG*), 2.2 ± 0.2 . Error bars represent SEM ($n = 6$).
- Wild type, 20.9 ± 1.5 (mean \pm SEM; $n = 9$); *atu* mutant, 27.0 ± 1.8 ($n = 8$); and DmDG-transgenic *atu* mutant (*atu/atu*; *actin5C-GAL4/UAS-DmDG*), 20.2 ± 1.2 ($n = 8$).
- Wild type, 15.7 ± 0.4 (mean \pm SEM); *atu* mutant, 32.3 ± 1.8 ; and DmDG-transgenic *atu* mutant (*atu/atu*; *actin5C-GAL4/UAS-DmDG*), 25.2 ± 1.6 ($n = 3$).
- Wild type, 124.9 ± 1.9 (mean \pm SEM; $n = 202$); *atu* mutant, 148.5 ± 2.3 ($n = 194$); and DmDG-transgenic *atu* mutant (*atu/atu*; *actin5C-GAL4/UAS-DmDG*), 115.5 ± 2.9 ($n = 119$).
- Wild type, 139.0 ± 4.7 (mean \pm SEM; $n = 98$); *atu* mutant, 151.8 ± 7.4 ($n = 88$); and DmDG-transgenic *atu* mutant (*atu/atu*; *actin5C-GAL4/UAS-DmDG*), 101.9 ± 6.3 ($n = 79$).
- We thank Y. Nakano for statistical analysis; H. Suzuki and J. Ikenouchi for assistance with electron microscopy; R. Niwa, M. O'Connor, A. P. Gould, and M. Kamakura for providing GAL4 flies; N. Juni for helpful discussions; A. Yamaguchi, Y. Yamaguchi, and M. Nishikawa for technical assistance; and R. Matsuda, H. Takeshima, Y. Nagai, and M. Ui for valuable advice and encouragement. This work was supported in part by Special Coordination Funds for Promoting Science and Technology from MEXT (Ministry of Education, Culture, Sports, Science and Technology), Japan, and by a research grant from The Novartis Foundation (Japan) for the Promotion of Science. D.Y. was supported by Specially Promoted Research grant 1802012 from MEXT and The Tohoku Neuroscience Global Centers of Excellence program.

Supporting Online Material

www.sciencemag.org/cgi/content/full/323/5922/1740/DC1

Materials and Methods

SOM Text

Figs. S1 to S11

Tables S1

References

9 September 2008; accepted 27 January 2009

10.1126/science.1165712

Quantitative 3D Video Microscopy of HIV Transfer Across T Cell Virological Synapses

Wolfgang Hübner,¹ Gregory P. McEnerney,³ Ping Chen,¹ Benjamin M. Dale,¹ Ronald E. Gordon,² Frank Y. S. Chuang,³ Xiao-Dong Li,⁴ David M. Asmuth,⁴ Thomas Huser,^{3,4} Benjamin K. Chen^{1*}

The spread of HIV between immune cells is greatly enhanced by cell-cell adhesions called virological synapses, although the underlying mechanisms have been unclear. With use of an infectious, fluorescent clone of HIV, we tracked the movement of Gag in live CD4 T cells and captured the direct translocation of HIV across the virological synapse. Quantitative, high-speed three-dimensional (3D) video microscopy revealed the rapid formation of micrometer-sized "buttons" containing oligomerized viral Gag protein. Electron microscopy showed that these buttons were packed with budding viral crescents. Viral transfer events were observed to form virus-laden internal compartments within target cells. Continuous time-lapse monitoring showed preferential infection through synapses. Thus, HIV dissemination may be enhanced by virological synapse-mediated cell adhesion coupled to viral endocytosis.

Human immunodeficiency virus (HIV) infection leads to depletion of CD4 T cells throughout the lymphoid system. Both cell-free and cell-associated infection routes contribute to viral dissemination in vivo (1). In vitro, infection with cell-associated HIV can be thousands fold more efficient than infection with cell-free virus (2), and inhibition of cell-cell contacts severely limits replication (3). Infection through

synapses between virus-carrying dendritic cells and CD4 T cells is highly efficient (4, 5). For human T cell lymphotropic virus type I, viral synapses between T cells are essential for dissemination (6). For HIV, infected and uninfected CD4 T cells form virological synapses that organize viral receptors CD4, CXCR4, and Env (7). These infectious contacts are regulated by cell adhesion through integrins and intercellular adhesion molecules (8),

dynamic actin and tubulin (9), cell signaling (10), and lipid raft recruitment (11). T cell virological synapses transfer virus with high efficiency (12), yet how this route fundamentally differs from cell-free infection remains unclear.

To examine the spatial and temporal organization of synapse formation, we used an infectious, fluorescent HIV clone, carrying a Gag-internal, interdomain insertion of the green fluorescent protein (GFP), called HIV Gag-iGFP (13). This virus faithfully reveals Gag localization, allowing infected cells and viral particles to be tracked with high sensitivity (12). Time-lapse fluorescence microscopy of virological synapse formation showed that 24% of HIV Gag-iGFP-expressing Jurkat cells formed stable adhesions to primary CD4 T cells within 4 hours (Fig. 1 and table S1A). After adhesion, 80% formed focal Gag accumulations at the contact site with an average 82-min interval (Fig. 1, A and B). In contrast, an Env-deficient clone was unable to induce cell-cell conjugates or Gag accumulation (table S1B), illustrating that adhesion precedes Gag redistribution.

¹Division of Infectious Diseases, Department of Medicine, Immunology Institute, Mount Sinai School of Medicine, New York, NY 10029, USA. ²Department of Pathology, Mount Sinai School of Medicine, New York, NY 10029, USA. ³NSF Center for Biophotonics Science and Technology, University of California Davis (UCD), Sacramento, CA 95817, USA. ⁴Department of Internal Medicine, University of California Davis Medical Center, Sacramento, CA 95817, USA.

*To whom correspondence should be addressed. E-mail: ben.chen@mssm.edu

In fixed samples, high-resolution confocal imaging revealed prominent Gag accumulations at the synapse (Fig. 1C). In three-dimensional (3D) reconstructions, these appeared as button-shaped discs, 1 to 3 μm in diameter (Fig. 1D and movie S1). Synaptic buttons were also observed in HIV Gag-iGFP-expressing primary CD4 T cells cocultured with homologous primary CD4 cells (fig. S1). We assessed viral assembly at the synapse by measuring Gag oligomerization with fluorescence resonance energy transfer (FRET) (13–15) between Cerulean and Venus variants of HIV Gag-iGFP, which form a donor-acceptor FRET pair (16). Excitation of the Cerulean donor in co-transfected Jurkat cells generated a robust Venus-shifted FRET signal at synaptic buttons that is indicative of Gag homo-oligomerization (Fig. 1E). Photobleaching the Venus acceptor at a synapse lead to increased donor emission, providing additional evidence for FRET (Fig. 1, F to H, and fig. S2). Three-dimensional reconstruction of FRET images revealed concentrated Gag oligomerization at synapses (movie S2).

With transmission electron microscopy, we observed that 100-nm budding viral crescents at the virological synapse protruded from the donor cell with bud tips directly abutting the target cell membrane (Fig. 1I). Viral buds were also observed far from the synapse, although at lower densities (fig. S3). Native, non-GFP-expressing HIV induced similar budding crescents, ruling out that GFP induced these accumulations (fig. S4). In thick 150-nm sections, near-complete viral buds and a virus-containing invagination in the synapsed target cell were observed (fig. S4, A and B).

To capture the dynamics of Gag trafficking, reorganization, and viral transfer with higher temporal and spatial resolution, we recorded high-speed, spinning disc confocal fluorescence images. Forty-three putative synaptic events encompassing 1187 min revealed dynamic Gag movements during virological synapse formation (table S2). New synaptic button formation ($n = 4$) was captured where patches of membrane-associated Gag moved toward the cell adhesion site within minutes (Fig. 2A and movie S3). At existing buttons, a ring-shaped zone of Gag depletion often surrounded the synaptic button (Fig. 2B), indicative of a synapse-proximal region from which Gag was recruited.

HIV Gag-iGFP-labeled structures ($n = 8$) close to existing buttons moved rapidly and directionally into the button (Fig. 2C, fig. S5, and movies S4 to S6). The structures moved into the synapse with average velocities of 0.10 to 0.25 $\mu\text{m}/\text{s}$ and peaks up to 0.8 $\mu\text{m}/\text{s}$ (Fig. 2C and fig. S5). Other small, mobile Gag puncta emerged from and then moved back into the synaptic button (Fig. 2D and movie S7). The fast, directional movement of Gag was seen predominantly from near-by puncta.

During cell-to-cell viral transfer ($n = 10$, table S2), fluorescent Gag signal protruded from buttons, penetrated the attached target cell, was

released into the target cell, and then migrated distally with a mean velocity of 0.12 $\mu\text{m}/\text{s}$ (Fig. 2E and movie S8). Notably, puncta 1.5 μm in diameter were observed (fig. S6A), and on occasion an entire synaptic button was transferred (movie S9). Large vesicular structures were also observed to fractionate into smaller vesicles while moving toward the distal pole of the cell (movies S4 and S8). The size of these translocated puncta

exceeds individual clathrin- or caveolin-associated structures, which are uniformly small (100 to 200 nm) (17). By using quantitative confocal microscopy, we found that the accumulation and maintenance of Gag puncta in target cells was remarkably stable over time (fig. S6, B to D, and movie S10).

The GFP signal in flow-sorted HIV+ CD4 target cells was uniformly punctate, without evidence

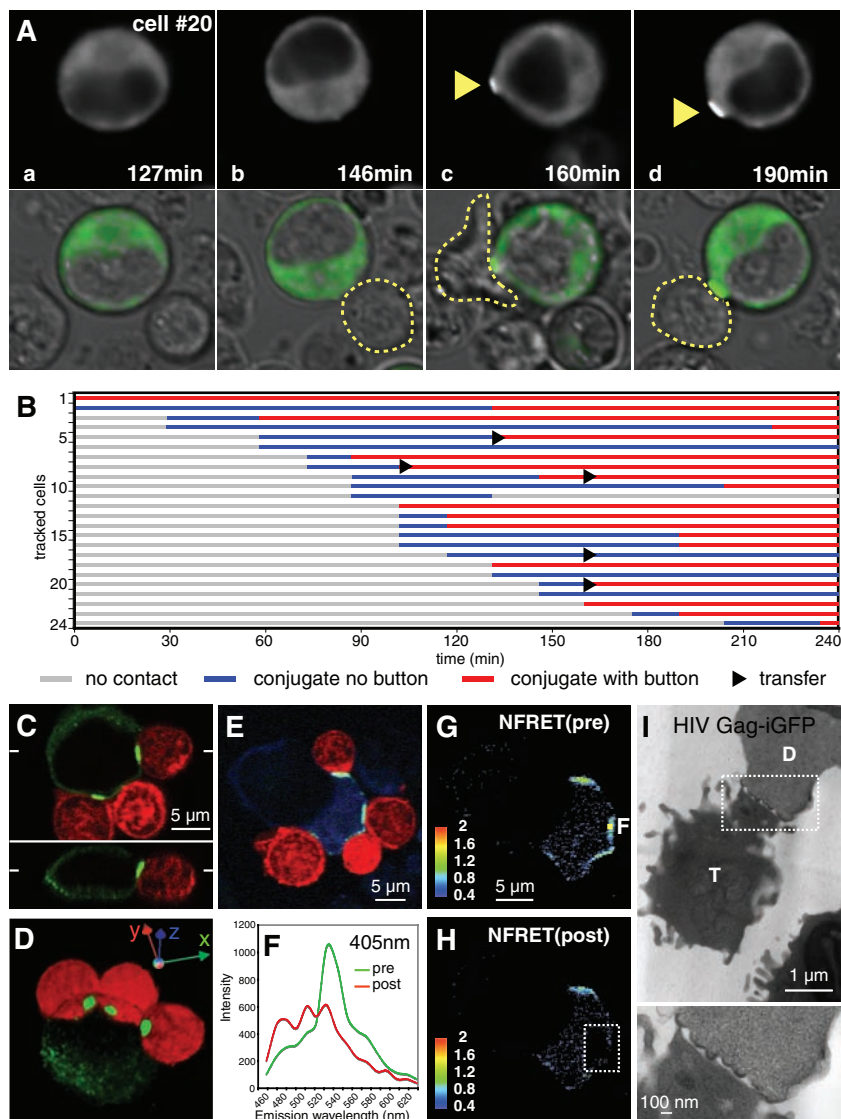


Fig. 1. Gag accumulates at synaptic buttons after T cell adhesion. (A) Time-lapse fluorescence imaging of synapse formation between an HIV Gag-iGFP-expressing Jurkat cell and a CD4 T cell. GFP image (top) and GFP/phase contrast overlay (bottom). Cells (a) before stable contact, (b) in stable adhesion (outlined), and (c and d) showing synaptic buttons (arrowheads). (B) Timing of synapse formation following 24 HIV+ Jurkat cells; each line represents an interactive cell. (C) Confocal fluorescence image of an HIV Gag-iGFP-expressing Jurkat T cell (green) synapsed with three primary CD4 T cells [red, labeled with CellTracker Orange CMRA (Invitrogen, Carlsbad, CA)]. Positioning of perpendicular planes marked at edges. (D) Reconstructed 3D view of (C). (E to H) FRET analysis of Gag-iCerulean (donor) and Gag-iVenus (acceptor) fluorophores at the synaptic button. (E) Three-color overlay donor Cerulean (blue, 405-nm excitation), FRET channel (green, 405-nm excitation), and target cells [red, 543-nm excitation stained with CellTracker Orange CMTMR (Invitrogen)]. (F) Emission spectra at synaptic button, point F, pre- and postacceptor photobleaching. (G and H) Normalized FRET (NFRET) signal (13) before and after acceptor photobleaching in boxed area. (I) Transmission electron micrographs of the synaptic junction between HIV Gag-iGFP-expressing donor, D, and target, T, cells. Low (top) and high (bottom) magnification of 70-nm sections.

of syncytia, and confocal imaging suggested that puncta were not surface-associated (fig. S7). Anti-Env staining of the Gag-iGFP puncta required cell permeabilization, indicating that Env was present in an internal Gag+ compartment (Fig. 2, F and G). Transmission electron microscopy of the target cells revealed multivesicular structures, which were not seen in control, unexposed cells, that contained viruslike densities inside 1- to 2- μm compartments (Fig. 2H). We conclude that synapses target HIV into vesicular compartments within recipient cells.

To track the fate of cells after synapse formation, we performed continuous, long-duration imaging. Jurkat donor cells were cotransfected with HIV Gag-iGFP and HIV NL-GI, an HIV molecular clone that expresses GFP in place of the viral early gene nef (18). This approach can visualize viral transfer (as puncta), as well as productive infection (as diffuse GFP) in the target cell. In

example one, the infected cell synapsed with the target cell for 18 hours, the cells separated, and at 32 hours a diffuse, bright GFP signal indicated productive infection (Fig. 3, A C, and movie S11). Bystander target cells remained negative. Over 67 hours, 112 conjugates tracked resulted in seven productively infected MT4 target cells (table S3). In five cases, synapses were observed, and in four cases virus transfer was recorded (Fig. 3, A to C, and movie S12). Under culture conditions that limited new cell-cell interactions, productively infected cells arose preferentially after observed virological synapse events.

Because synapse-mediated viral transfer is coreceptor-independent (12, 19), we tested whether infection through T cell synapses requires coreceptor expression. Infection of MT4 cells by cell-associated HIV was inhibited when cells were separated by a 0.4- μm transwell barrier (Fig. 4A).

Under these contact-dependent infection conditions, productive infection by cell-associated HIV NL-GI was inhibited by CXCR4-antagonist, AMD3100 (Fig. 4B). Furthermore, productive infection by cell-associated R5-tropic virus HIV NL-GI (JRFL) was dependent on expression of the chemokine receptor, CCR5 (Fig. 4C). The results suggest that infection through T cell synapses does not bypass the coreceptor requirement.

Synapse-mediated viral transfer is potentially inhibited by actin inhibitors such as cytochalasin D (9, 12). We find that cytochalasin D had little effect on cell-free HIV infection yet effectively inhibited productive infection by cell-associated HIV (Fig. 4D). Additionally, a well-characterized patient antisera, which can potentially block cell-free infection but not transfer of virus through virological synapses (12), did not efficiently block infection of the homologous cell-associated

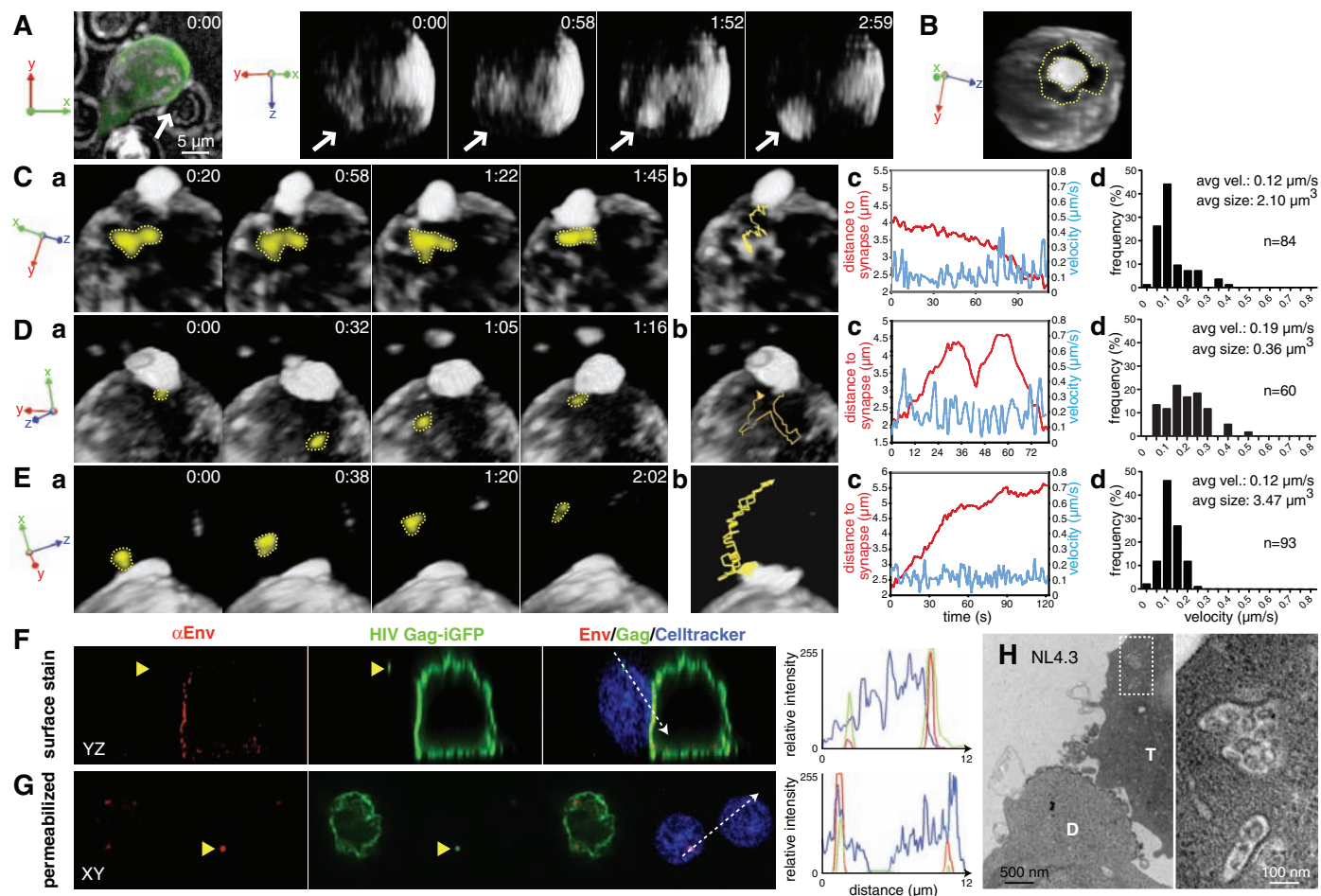


Fig. 2. Dynamic recruitment of Gag puncta to the synapse and viral transfer into a target cell compartment revealed with rapid spinning-disc 3D confocal fluorescence microscopy. (A) Formation of a buttonlike accumulation of Gag at the site of adhesion, z projection at time = 0 (left), selected 3D reconstructions of contact site (arrows) over time (right four images). (B) A zone of Gag depletion, 2 to 3 μm wide, surrounds the synaptic button (dotted yellow line). (C) Patches of synapse-proximal Gag merge into the synapse. (D) A Gag-iGFP puncta moves out of and into the synapse. (E) During a transfer event, Gag puncta emerge from the synapse, separate, and then move to the distal pole. In (C) to (E), (a) selected frames highlight movement of Gag-iGFP puncta (yellow). (b) Object path is overlaid on the initial image. (c) Object distance

to the synapse center and relative velocity are graphed over time. (d) Histogram distribution of the tracked objects velocities. (F and G) Immunostaining of Gag puncta requires membrane permeabilization. (F) Nonpermeabilized, anti-Env immunostain (red) does not stain the Gag-iGFP+ puncta (green) within the CD4 target cell (CellTracker Blue CMF2HC, Invitrogen), whereas surface Env-staining at synapse is observed. Three-color intensity profile along the 12- μm line (right). (G) Permeabilization of fixed cells reveals anti-Env immunostain (red) at the GFP puncta (green) within the CD4 target cell (blue). (H) Transmission electron micrograph of vesicles containing corelike structures in a CD4 cell engaged in synapse with an HIV-infected Jurkat cell. Low (left) and high (right) magnification of 70-nm sections.

virus (Fig. 4E). Thus, inhibitor studies clearly distinguish the mechanisms of cell-free from those of cell-associated infection.

The live imaging of HIV cell-to-cell transfer reveals that dynamic Gag movements in infected cells organize Gag puncta into synaptic buttons

from which HIV is directly transferred into adjacent target cells. Although endocytic entry of cell-free HIV contributes only modestly to productive

Fig. 3. Productive infection of synapsed cells is visualized by 72-hour imaging of immobilized cells engaged in virological synapse. (A) Donor cells cotransfected with HIV Gag-iGFP to track viral transfer and HIV NL-GI to visualize new early gene expression in target cells. Images show a synapsed pair where the target cell (number 1) separates from donor at 18 hours and expresses increasing levels of diffuse GFP at 32 hours. Top row shows GFP images; bottom, GFP/phase overlays. (B) Four examples of synapsed MT4 target cells that subsequently expressed HIV (numbers 2 to 5). (C) Fluorescence intensity of the target cells 1 to 7. Numbers 6 and 7 are control bystander cells. Duration of cell contact indicated on bottom.

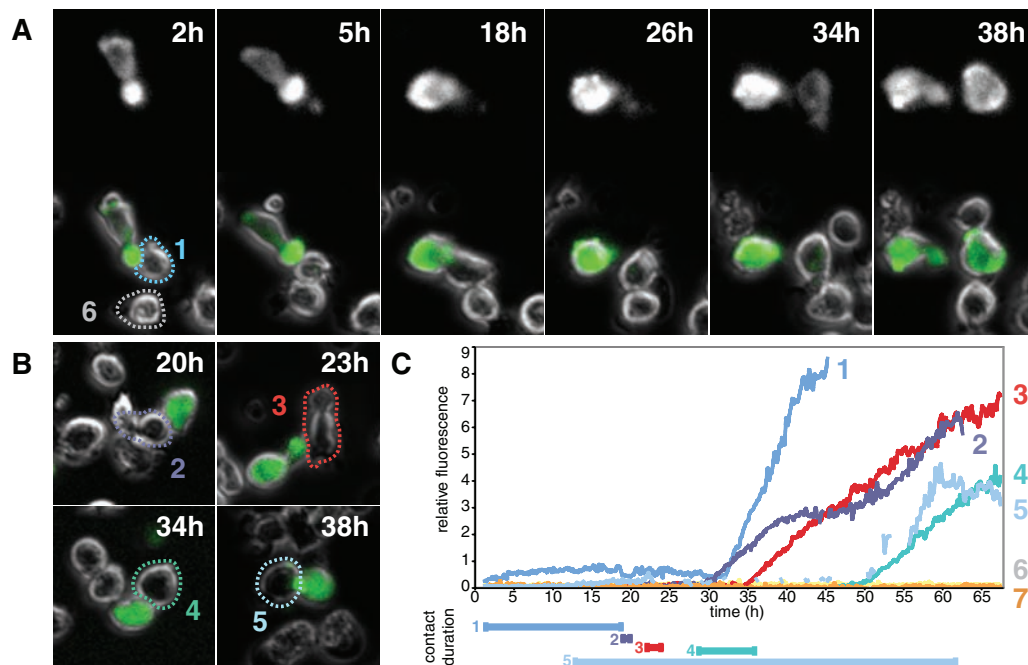
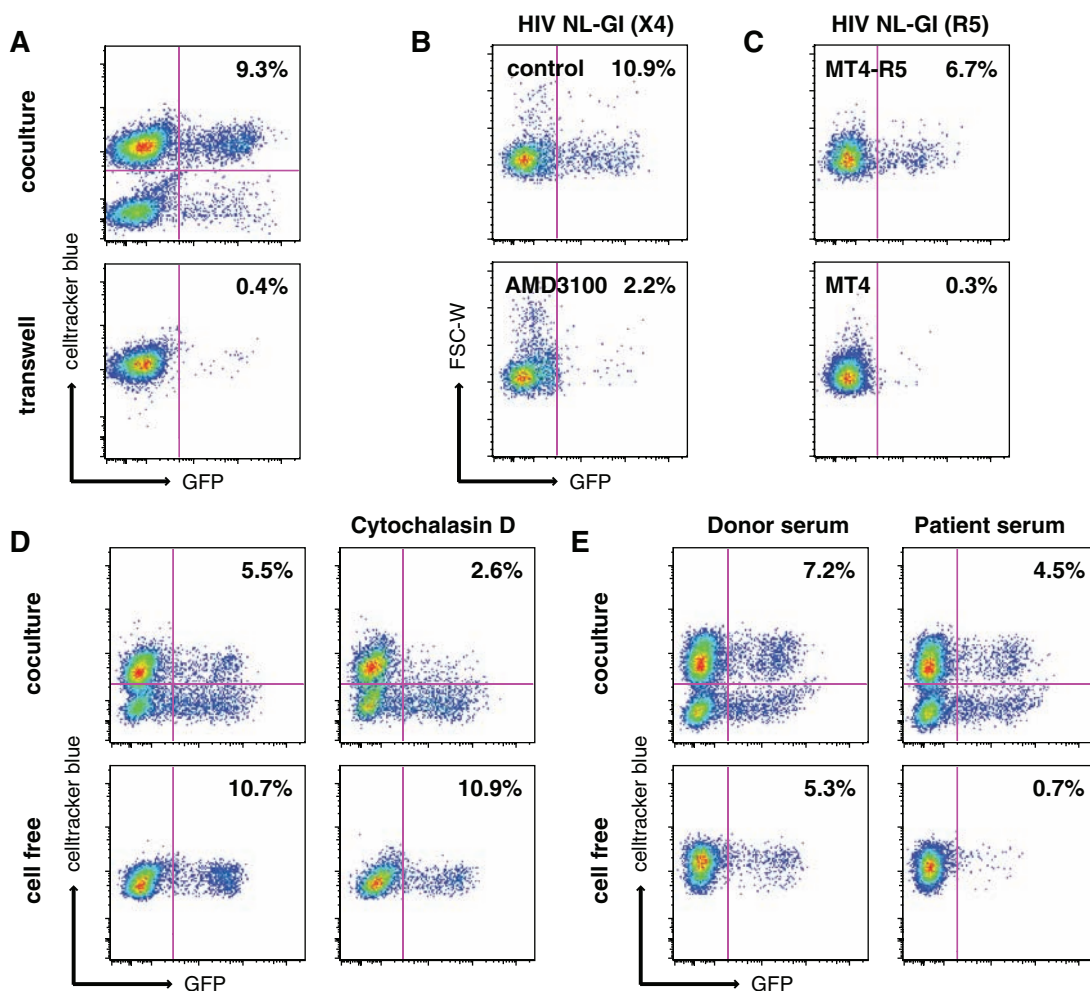


Fig. 4. Cell-associated infection is coreceptor-dependent and actin-dependent and can resist a neutralizing antiserum. (A) HIV NL-GI-expressing Jurkat cells were cocultured with CellTracker Blue CMF2HC-labeled MT4 cells in the absence or the presence of a 0.4- μ m transwell barrier between cells. Productive infection (GFP expression) in CellTracker-labeled target cells was measured by flow cytometry at 48 hours. (B) Coreceptor antagonist AMD3100 (10 μ g/ml) inhibits infection of target cells by cell-associated X4-tropic virus, HIV NL-GI, at 48 hours. Productive infection in gated target cells indicated by GFP expression and is plotted against forward scatter width (FSC-W). (C) Cell-associated R5-tropic virus infects CCR5-expressing MT4 cells but not CCR5-negative MT4 cells. Jurkat cells expressing R5-tropic HIV NL-GI(JRFL) were donor cells. (D) Cytochalasin D (2.5 μ M) inhibits cell-associated infection (top) but fails to block infection with cell-free virus (bottom). (E) A neutralizing antiserum that blocks cell-free infection (bottom) is less effective at blocking homologous cell-associated infection (top). Results representative of at least three independent experiments.



infection (20–22), our results suggest that the cell-to-cell transmission could favor endocytic routes. Thus when spreading via synapses, it is possible that HIV resembles a majority of viruses that enter preferentially through endocytosis (e.g., influenza, adenoviruses, picornaviruses, alphaviruses) (23). Given this scenario, the tight coupling of Env fusogenicity with particle maturation (24, 25) may activate viral fusion within a target cell compartment that is cloistered from neutralizing antibodies (12). Alternatively, the prominent endocytic process that accompanies synapse formation may create viral reservoirs in intracellular compartments.

Future vaccine strategies may be focused against unique cell-surface Env epitopes that block cell-associated infection, and future antiviral drugs may target factors required for synapse formation. Ultimately the dynamics of virological synapse formation must be understood within lymphoid tissues, where high density and lymphocyte mobility (26) are likely to promote synaptic viral spread.

References and Notes

- A. T. Haase, *Nat. Rev. Immunol.* **5**, 783 (2005).
- D. S. Dimitrov *et al.*, *J. Virol.* **67**, 2182 (1993).
- M. Sourisseau, N. Sol-Foulon, F. Porrot, F. Blanchet, O. Schwartz, *J. Virol.* **81**, 1000 (2007).
- P. U. Cameron *et al.*, *Science* **257**, 383 (1992).
- D. McDonald *et al.*, *Science* **300**, 1295 (2003); published online 1 May 2003 (10.1126/science.1084238).
- T. Igakura *et al.*, *Science* **299**, 1713 (2003); published online 13 February 2003 (10.1126/science.1080115).
- C. Jolly, K. Kashefi, M. Hollinshead, Q. J. Sattentau, *J. Exp. Med.* **199**, 283 (2004).
- C. Jolly, I. Mitar, Q. J. Sattentau, *J. Virol.* **81**, 13916 (2007).
- C. Jolly, I. Mitar, Q. J. Sattentau, *J. Virol.* **81**, 5547 (2007).
- N. Sol-Foulon *et al.*, *EMBO J.* **26**, 516 (2007).
- C. Jolly, Q. J. Sattentau, *J. Virol.* **79**, 12088 (2005).
- P. Chen, W. Hubner, M. A. Spinelli, B. K. Chen, *J. Virol.* **81**, 12582 (2007).
- W. Hubner *et al.*, *J. Virol.* **81**, 12596 (2007).
- A. Derdowski, L. Ding, P. Spearman, *J. Virol.* **78**, 1230 (2004).
- D. R. Larson, Y. M. Ma, V. M. Vogt, W. W. Webb, *J. Cell Biol.* **162**, 1233 (2003).
- M. A. Rizzo, G. H. Springer, B. Granada, D. W. Piston, *Nat. Biotechnol.* **22**, 445 (2004).
- M. Lakadamyali, M. J. Rust, X. Zhuang, *Cell* **124**, 997 (2006).
- G. B. Cohen *et al.*, *Immunity* **10**, 661 (1999).
- J. Blanco *et al.*, *J. Biol. Chem.* **279**, 51305 (2004).
- O. T. Fackler, B. M. Peterlin, *Curr. Biol.* **10**, 1005 (2000).
- V. Marechal *et al.*, *J. Virol.* **75**, 11166 (2001).
- E. Schaeffer, V. B. Soros, W. C. Greene, *J. Virol.* **78**, 1375 (2004).
- M. Marsh, A. Helenius, *Cell* **124**, 729 (2006).
- D. J. Wyma *et al.*, *J. Virol.* **78**, 3429 (2004).
- S. Wyss *et al.*, *J. Virol.* **79**, 12231 (2005).
- R. N. Germain, M. J. Miller, M. L. Dustin, M. C. Nussenzweig, *Nat. Rev. Immunol.* **6**, 497 (2006).
- We thank R. H. Cheng, V. Simon, M. Klotman, R. Iyengar, and A. Del Portillo for critiques and discussions; R. Huq for microscopy support; S. Izadmehr for image analysis; M. Grisotto and V. Sahi for cell sorting; H. Bell for electron microscopy support; and S. Lira for imaging support. Work was supported by NIH grant AI074420-02, Burroughs Wellcome Fund Investigator Award, and Hirschl Weill-Caulier Career Scientist Award to B.K.C. Imaging was supported by Mount Sinai School of Medicine–Microscopy Shared Resource Facility grants NIH-NCI 5R24 CA095823-04, NSF-DBI-9724504, and NIH-S10RR09145-01; by the NSF Center for Biophotonics Science and Technology (cooperative agreement PHY012099); a UCD Health System Research Award to T.H.; and the UCD Clinical and Translational Science Center grant NIH-NCRR ULRR024146 (T.H. and D.M.A.).

Supporting Online Material

www.sciencemag.org/cgi/content/full/323/5922/1743/DC1
Materials and Methods
Figs. S1 to S7
Tables S1 to S3
Movies S1 to S12

22 October 2008; accepted 30 January 2009
10.1126/science.1167525

A Transposon-Based Genetic Screen in Mice Identifies Genes Altered in Colorectal Cancer

Timothy K. Starr,^{1*} Raha Allaei,¹ Kevin A. T. Silverstein,² Rodney A. Staggs,² Aaron L. Sarver,² Tracy L. Bergemann,³ Mihir Gupta,⁴ M. Gerard O'Sullivan,⁵ Ilze Matise,⁵ Adam J. Dupuy,⁶ Lara S. Collier,⁷ Scott Powers,⁸ Ann L. Oberg,⁹ Yan W. Asmann,⁹ Stephen N. Thibodeau,⁹ Lino Tessarollo,¹⁰ Neal G. Copeland,¹¹ Nancy A. Jenkins,¹¹ Robert T. Cormier,¹² David A. Largaespada^{1*}

Human colorectal cancers (CRCs) display a large number of genetic and epigenetic alterations, some of which are causally involved in tumorigenesis (drivers) and others that have little functional impact (passengers). To help distinguish between these two classes of alterations, we used a transposon-based genetic screen in mice to identify candidate genes for CRC. Mice harboring mutagenic Sleeping Beauty (SB) transposons were crossed with mice expressing SB transposase in gastrointestinal tract epithelium. Most of the offspring developed intestinal lesions, including intraepithelial neoplasia, adenomas, and adenocarcinomas. Analysis of over 16,000 transposon insertions identified 77 candidate CRC genes, 60 of which are mutated and/or dysregulated in human CRC and thus are most likely to drive tumorigenesis. These genes include *APC*, *PTEN*, and *SMAD4*. The screen also identified 17 candidate genes that had not previously been implicated in CRC, including *POLI*, *PTPRK*, and *RSPO2*.

Recent genomic studies have revealed that human colorectal cancers (CRCs) undergo numerous genetic and epigenetic alterations (1–4). These alterations probably derive from a mixture of “drivers” that play a causal role in tumor formation and progression and “passengers” that have little or no effect on tumor growth. The design of targeted therapeutics for CRCs is dependent on the ability to distinguish drivers from passengers.

To help identify potential driver genes in CRC, we developed a forward genetic screen in mice by using a Sleeping Beauty (SB) system to generate insertional mutations. To confine transposition to the gastrointestinal tract, SB11 transposase cDNA, preceded by a LoxP-flanked stop cassette, was knocked into the *Rosa26* locus (fig. S1) (5). These mice were then crossed with *Villin-Cre* transgenic mice to activate SB transposase in epithelial cells of the gastrointestinal tract (6). Once ex-

pressed, SB transposase catalyzed the transposition of *T2/Onc*, a mutagenic SB transposon (Fig. 1A) (7). *T2/Onc* contains a murine stem-cell virus long terminal repeat and splice donor site (MSCV-LTR-SD), which can deregulate the expression of a nearby proto-oncogene. *T2/Onc* also carries splice acceptor sites in both DNA strands and a bidirectional polyadenylate signal, which can inactivate the expression of a tumor suppressor gene. Because SB transposition is biased toward reintegration of the transposon into the same chromosome as the donor transposon (a phenomenon referred to as “local hopping”), we used two *T2/Onc* transgenic lines that each carried approximately 25 copies of the *T2/Onc* transposon in a concatamer on different donor chromosomes (chrs 1 and 15) (7).

A histochemical analysis of the triple transgenic mice (*Rosa26-LsL-SB11*, *T2/Onc*, and *Villin-Cre*) showed that SB transposase was strongly expressed in epithelial cells of the gut and pancreas but undetectable in other tissues (fig. S2). We created a cohort of 28 triple transgenic mice and 72 double transgenic control mice carrying all possible dual combinations of the three transgenes. Mice in this first cohort were monitored daily for 18 months. We generated a second cohort of 50 triple transgenic mice that were maintained in a separate facility for 12 months and also monitored daily.

Triple transgenic mice died at a faster rate than double transgenic controls, beginning around one year of age (Fig. 1B). Examination of the gastrointestinal tract of moribund animals revealed discrete raised lesions ranging from 2 mm to as large as 5 mm in diameter in the small and large intestine. In the first cohort, 100% (12 out of 12)